Case Studies in Thermal Engineering 51 (2023) 103559

Contents lists available at ScienceDirect

Case Studies in Thermal Engineering

journal homepage: www.elsevier.com/locate/csite

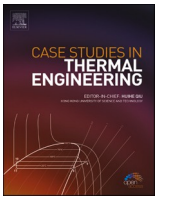

Proposal of a microchannel receiver for Fresnel technology to supply solar heat for industrial processes

M.J. Montes [a,*], V. Stojceska [b], D. Reay [c], M. Ibarra [a]

[a] E.T.S. Ingenieros Industriales - UNED, C/Juan del Rosal 12, 28040, Madrid, Spain
[b] Brunel University, London, United Kingdom
[c] David Reay and Associates, Whitley Bay, United Kingdom

ARTICLE INFO

Keywords:
Linear fresnel reflector
Solar heat for industrial processes
Microchannel receiver
Convergent absorber panels
Light-trapping geometry
Pressurised gases

ABSTRACT

This work is focused on the linear Fresnel technology to supply solar heat for industrial processes, proposing a new microchannel receiver design for pressurised gases. This design consists of two absorber panels converging at the focal line of the Fresnel system; each of these panels consists of a compact core fin structure attached to both front and back plates. The fluid flows through the receiver along its length in several passes, so that the compactness is constant and greater than in the previous pass. This arrangement improves heat transfer and, therefore, the cooling of the more thermally stressed areas of the panel, without over penalising the pressure drop.

A thermal resistance model has been formulated to quantify the fluid heating along the panel length and the thermal gradient along the panel thickness. This model has been used to perform a thermo-exergy optimisation based on several characteristic parameters: the aperture half-angle of the cavity shaped by the two converging panels; and the channels dimensions in each pass of the panel. For each of these parameters, a maximum exergy efficiency has been obtained accounting for the receiver heat losses, the fluid pressure drop and the optical performance of the primary mirror field.

Acronyms

CPC	Compound Parabolic Concentrator
CHE	Compact Heat Exchanger
CFD	Computational Fluid Dynamics
HCE	Heat Control Element
HTF	Heat Transfer Fluid
HX	Heat Exchanger
LFC	Linear Fresnel Collector
NREL	National Renewable Energy Laboratory
PCHE	Printed Circuit Heat Exchanger
PFHE	Plate Fin Heat Exchanger
PHE	Plate Heat Exchanger

* Corresponding author.
E-mail address: mjmontes@ind.uned.es (M.J. Montes).

https://doi.org/10.1016/j.csite.2023.103559
Received 15 March 2023; Received in revised form 27 September 2023; Accepted 27 September 2023
Available online 28 September 2023

PTC	Parabolic Trough Collector
sCO_2	Supercritical Carbon Dioxide
SHIP	Solar Heat for Industrial Processes
STPP	Solar Thermal Power Plant
TRM	Thermal Resistance Model

NotationLatin letters

F	View factor
h	Specific enthalpy (J kg^{-1})
h_{conv}	Convection heat transfer coefficient (W m^{-2} K^{-1})
k	Thermal conductivity (W m^{-1} K^{-1})
L	Length (m)
$\dot{m}$	Mass flow rate (kg s^{-1})
N	Number of channels
ΔP	Pressure drop (Pa)
P	Pressure (Pa)
$\dot{Q}$	Thermal power (W)
R	Thermal resistance (K W^{-1})/Ideal gas constant (J kg^{-1} K^{-1})
Re	Reynolds number
T	Temperature (K)
t	Thickness (m)
v	Velocity (m s^{-1})
W	Width (m)

Greek Letters

η	Efficiency
Δ	Differential
ρ	Density (kg m^{-3})

Subscripts

amb	Ambient
cond	Conduction
conv	Convection
ex	Exergy
f	Fin
in	Inlet
LMTD	Logarithmic mean temperature difference
loss	Loss
opt	Optical
out	Outlet/outside
p	Intermediate plate/pressure
p0	Frontal plate
rad	Radiation
rec	Receiver
ref	Reflection
th	Thermal

1. Introduction

In the present energy context, the gradual replacement of fossil fuels by alternative energy sources is necessary. One of the sectors where there is a greatest demand for fossil-fuelled thermal energy is industry. In this scenario, Solar Heat for Industrial Processes (SHIP) becomes a promising way of supplying renewable heat to the industrial sector, while also promoting the development of the solar technology [1].

Based on the working temperature, SHIP applications can be divided into low temperature ($T < 100\ ^{\circ}C$), medium temperature ($100\ ^{\circ}C < T < 250\ ^{\circ}C$) or high temperature processes ($250\ ^{\circ}C < T < 400\ ^{\circ}C$). For each temperature, there is a solar collector technology that is best suited to the industrial application. In particular, linear solar collectors are intended to provide heat in medium and high temperature ranges ($100\ ^{\circ}C < T < 400\ ^{\circ}C$), being the more common technologies Parabolic Trough Collector (PTC) and Linear Fresnel Collector (LFC) [2]. Compared to PTC, LFC has significant cost reduction potential, mainly due to cheaper mirrors and structural advantages. In the case of PTC, the concentrator mirror is a cylinder with a parabolic cross-section. In the case of the LFC, the concentrating mirror is discretised into an array of linear reflectors whose cross-section is straight, cylindrical or even parabolic in

shape, with a single-axis solar tracking system frame. These primary reflectors behave optically as a single unit, as they are all oriented to reflect the sun's rays towards the same focal line, where the receiver is located.

The state-of-art on the receiver for LFC shows that there are two different design concepts: the single-tube and the multi-tube receiver.

The single-tube receiver consists of a single tube, typically located inside a CPC (Compound Parabolic Concentrator) cavity, which performs as a secondary reflector [3]. The current conventional design for this receiver is an evacuated tube with CPC, which has demonstrated to have the highest annual thermal performance, compared to other non-evacuated single tube proposals, or even the PTC receiver [4]. The standard size of the tube diameter is 70 mm, as this size minimises the electricity cost for LFCs in Solar Thermal Power Plants (STPPs) [5]. This receiver is also used by several LFCs for process heat, such as the LF-11 collector [6].

The multi-tube receiver consists of several parallel tubes arranged horizontally in a trapezoidal-shaped cavity [7]. The cavity opening can be provided with a glass cover, which aims both to reduce heat loss and to create a greenhouse effect inside the cavity, improving the thermal performance of the receiver. However, the high temperature of the glass plate can cause significant technical drawbacks. Therefore, research has focused on selective coatings for the tubes that do not degrade in contact with air at ambient pressure [8]. Multitube receivers have been employed in the Kimberlina and Dhursar plants [5] using thermal oil as the heat transfer fluid.

In comparison to the two designs described above, this paper analyses a new concept of receiver: the microchannel receiver for pressurised gas as working fluid. Such receivers have already been proposed for central tower systems [9]. They are based on Compact Heat Exchanger (CHE) structures, with the most suitable for the new generation of solar receivers being Plate Heat Exchanger (PHE), Plate-Fin Heat Exchanger (PFHE), Printed Circuit Heat Exchanger (PCHE) and ceramic heat exchanger designs. Several simulation models, reviews and prototypes have been proposed in the technical literature, but all of them applied to central solar receivers [10–12].

Nevertheless, as explained in Refs. [13,14], the main drawback of these receivers lies in the need for materials that can withstand the high operating temperatures (above 700 °C). Such materials, like stainless steel, nickel and even titanium alloys [15], have the disadvantage of low thermal conductivity, which leads to high temperature gradients along the compact structure thickness, with non-uniform heating of the microchannel rows, parallel in the direction of the solar flux. The use of these receivers in LFCs working at lower temperatures (for medium and high temperature industrial process heat), allows the use of materials with higher conductivity, which would improve the heat transfer, performing as a finned structure.

This work proposes an original microchannel receiver design for pressurised gases, which consists of two absorber panels converging in the focus line of the LFC; each panel is a plate–fin compact structure with a gradual compactness concept [16], as depicted in Figs. 1 and 2. The two main advantages of this design are described as follows. Firstly, the pseudo-cavity with a triangular cross-section shaped by the two converging panels performs as a macroscopic light-trapping geometry. With an appropriate aiming strategy, the area with the highest concentrated solar flux and thus the highest surface temperature, matches the inner area of the panel, close to the receiver axis. As the view factor from the absorber panel surface towards the outside is reduced as it approaches the receiver axis, heat losses are also reduced. Secondly, the gradual compactness concept consists of decreasing the hydraulic diameter of the compact structure as the fluid is heated. Hence, as shown in Fig. 1, for a two-pass receiver, the second pass has a smaller hydraulic diameter and a higher Reynolds number than the first pass. In this way, heat transfer improvement is limited to the panel area affected by the worse cooling conditions (hotter fluid and a higher concentrated solar flux), without excessively penalising pressure drop.

To conclude this introduction, it can be stated that there are not many prototypes or studies in technical literature regarding the use of pressurised gases as working fluid in concentrated solar receivers. The existing references mainly concern the previously described central receiver prototypes. In the case of receivers for linear concentrating collectors, test loops [17], and studies for commercial plants [18] have been conducted, always using the conventional evacuated single-tube receiver design. This work provides innovation by proposing a specific receiver design for pressurised gases in Fresnel collectors. This design is based on a compact finned structure to

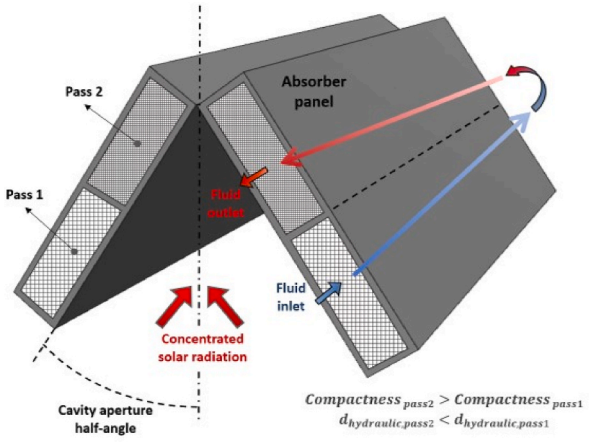

Fig. 1. Scheme of the microchannel linear solar receiver analysed in this work.

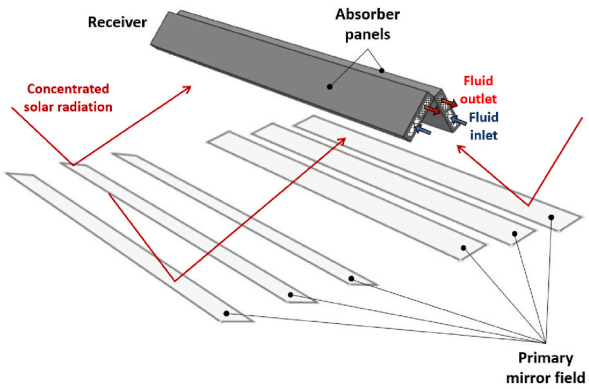

Fig. 2. Scheme of the LFC in which the microchannel linear solar receiver is included.

increase the heat transfer area to the fluid. In addition, this receiver concept achieves reduced heat losses due to the arrangement of the panels in a triangular cross-section cavity, and reduced pressure drop by adjusting the channel hydraulic diameter to the panel cooling requirement. Both features improve the receiver exergy efficiency.

This paper deals with the analysis and thermal optimisation of this new microchannel receiver design for LFC, according to the following structure. Firstly, the methodology section introduces a brief description of the heat transfer model characterising the receiver; then, the boundary conditions of the receiver, both optical (coupling to the mirror field) and thermal (coupled to the industrial processes) are defined; finally, the objective function to be optimised is identified: the global exergy efficiency referring to the solar subsystem. Two representative optimisation analyses are studied in the results section. The first analysis studies the aperture of the cavity, accounting for the optics and the thermal performance. The second one focuses on the effect of the gradual compactness in the microchannel structure. The main conclusions and future works are summarised in the last section.

2. Engineering analysis

2.1. Thermo-fluid model of the microchannel receiver

The thermal model used to characterise this receiver is similar the one previously developed for solar central receivers [12]. As can be seen in Fig. 3, there are two main heat transfer paths within the microchannel panel. Firstly, there is a fluid heating along the flow direction, which is characterised by an energy balance in that direction; in addition, there is a thermal gradient along the panel thickness, which causes the heating of the channel rows to be non-uniform in that direction. Both heat transfer models, implemented in Matlab [19], have to be considered in order to calculate the external temperature of the panel and, consequently, the heat losses to the outside. These models have been thoroughly described in Ref. [12], and the main equations are summarised below.

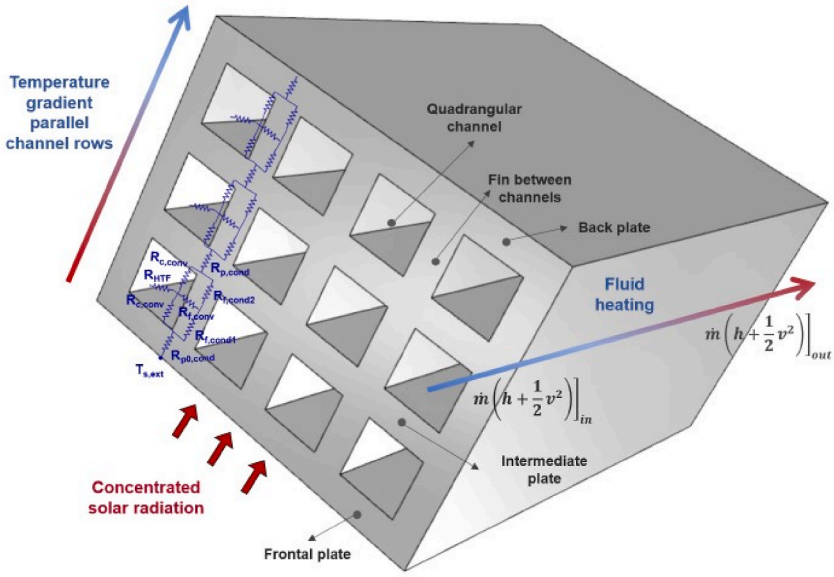

Fig. 3. Thermal resistance circuit to model the heat transfer in the compact structure of the absorber panel.

The fluid heating along the flow direction is characterised by an energy balance for each of the Heat Control Elements (HCEs) into which the receiver is divided in that direction. This energy balance is summarised in the following Eqs. (1)–(3).

$$\dot{Q}_{solar}|_{HCE} = \dot{Q}_{abs}|_{HCE} + \dot{Q}_{loss,ref}|_{HCE} \tag{1}$$

$$\dot{Q}_{abs}|_{HCE} = \dot{Q}_{conv,HTF}|_{HCE} + \dot{Q}_{loss,conv}|_{HCE} + \dot{Q}_{loss,rad}|_{HCE} \tag{2}$$

$$\dot{Q}_{loss}|_{HCE} = \dot{Q}_{loss,rad}|_{HCE} + \dot{Q}_{loss,ref}|_{HCE} + \dot{Q}_{loss,conv}|_{HCE} \tag{3}$$

In the above equations, $\dot{Q}_{solar}$ is the concentrated solar radiation, from the primary mirror field, that impinges the receiver surface. $\dot{Q}_{abs}$ accounts for the part of this energy that is absorbed by the receiver, to be transferred by conduction through its thickness and finally by convection to the fluid. $\dot{Q}_{conv,HTF}$ is the heat gain by convection to the fluid, and its calculation depends on the fluid regime: for turbulent flow, Gnielinski correlation is used [20]; for laminar flow, a constant value is recommended [20]; at last, interpolation between both values is used in the transitional region. $\dot{Q}_{loss}$ account for the heat losses from the receiver, by radiation ($\dot{Q}_{loss,rad}$), convection ($\dot{Q}_{loss,conv}$) and reflection ($\dot{Q}_{loss,ref}$). Radiation and reflection heat losses are calculated by means of the Stefan-Boltzmann equation, considering the infrared or solar emissivity of the absorber panel external surface, as well as the view factor between this surface and the cavity aperture [12]. Convection heat loss is estimated using Siebers and Kraabel correlation [12].

The temperature gradient along the panel thickness is characterised by a thermal resistance model, whose equivalent overall thermal resistance is given by Eq. (4).

$$R_{th,panel} = R_{p0,cond} + \frac{N_{c,rows}}{2}\left[R_{p,cond} + \left\{R_{c,conv} \parallel \left(R_{f,cond} + \left(\left(R_{f,cond} + R_{c,conv}\right) \parallel R_{f,conv}\right)\right)\right\} + R_{HTF}\right] \tag{4}$$

In Eq. (4), $N_{c,rows}$ is the number of parallel channel rows in the absorber panel; and the thermal resistances appearing in this equation are described in Table 1.

In Table 1, t_p is the intermediate plate thickness (t_{p0} for frontal plate); t_f and l_f are the fin thickness and length, respectively; L_{HCE} and W_{HCE} are the HCE length and width, respectively; ρ, c_p and v are the average fluid density, specific heat and velocity in each HCE; k_{rec} is the absorber thermal conductivity; and h_{conv} is the convection heat transfer coefficient to the fluid.

It is assumed that the fluid flows along the receiver length, and returns in reverse, thus completing two flow passes through the absorber panel. It enters first the outer flow section of the panel, which is close to the receiver aperture, and exits through the inner flow section, the one close to the receiver axis. Although there are many compact structure geometries [20], the simplest case of plain rectangular fin and quadrangular section is considered; in this way, the hydraulic diameter matches one side of the quadrangular wetted perimeter.

The receiver uses pressurised CO_2 as the working fluid, which has better thermal properties than pressurised air [14]. This reduces the receiver length required to achieving the same temperature increment and, consequently, the fluid pressure drop. The CO_2 thermodynamic properties in the receiver's working region have been obtained from the NIST database [21], using temperature steps below 0.4 °C and pressure steps equal to 0.05 bar.

Since the working temperature is medium-high, the material selected for the core fin is a aluminium alloy (k = 190 W/m/°C).The frontal plate, exposed to the concentrated solar flux, is made of a ferritic alloy (k = 36 W/m/°C), with an air-stable solar selective coating that has a solar absorptivity equal to 0.96 and a thermal emissivity of 0.3 [22]. Table 2 shows the main geometrical parameters selected for the receiver.

In Table 2, the cavity aperture half-angle is referred to as the angle between the absorber panel and the vertical, as shown in Fig. 1. This angle is one of the main geometrical parameters analysed in this work, since it affects simultaneously to the optical and the thermal performance of the LCF receiver, as explained in the results section.

2.2. Thermal and optical boundary conditions

It is considered that each LFC supplies 0.1 MW_{th} to a generic industrial process; for this thermal power, it is also considered two

Table 1
Thermal resistances included in the calculation of the temperature gradient along the panel thickness.

Symbol	Description	Expression
$R_{p,cond}$	Thermal resistance due to conduction through the wall thickness of the intermediate (frontal) plate	$R_{p,cond} = \frac{t_p}{k_{rec} \cdot W_{HCE} \cdot L_{HCE}}$
$R_{c,conv}$	Thermal resistance due to convection between the channel base and top surface	$R_{c,conv} = \frac{1}{h_{conv} \cdot W_{HCE} \cdot L_{HCE}}$
$R_{f,cond}$	Thermal resistance due to conduction through the fin half length	$R_{f,cond} = \frac{\left(\frac{l_f}{2}\right)}{k_{rec} \cdot t_f \cdot L_{HCE}}$.
$R_{f,conv}$	Thermal resistance due to convection from the fin surface to the fluid	$R_{f,conv} = \frac{1}{2 \cdot l_f \cdot h_{conv} \cdot L_{HCE}}$
R_{HTF}	Thermal resistance due to the fluid heat gain	$R_{HTF} = \frac{1}{\rho \cdot c_p \cdot v \cdot W_{HCE} \cdot L_{HCE}}$

Table 2
Themo-fluid and geometrical parameters of the receiver (*These parameters are optimised in section 3.1).

Global characteristics of the absorber panel	
Thermal fluid	Pressurised CO2 (25 bar)
Core fin material	Aluminum 3003 Alloy (k = 190 W/m/°C)
Frontal plate material	SA335 P22 Alloy (k = 36 W/m/°C)
Number of flow passes in the panel	2
Compact structure	Plain rectangular fin
Channel shape	Quadrangular
Cavity aperture half-angle*	10° - 90° (Horizontal)
Pass 1	
Channel side (mm)*	7–12
Number of channel rows along panel thickness	6
Number of channel rows along pass 1 width	16
Number of channel rows along pass 2 width	25
Plate thickness (mm)	1
Thickness between channels (mm)	3
Frontal plate thickness (mm)	1.5
Pass 2	
Channel side (mm)*	4–9
Number of channel rows along panel thickness	6
Number of channel rows along pass 1 width	16
Number of channel rows along pass 2 width	25
Plate thickness (mm)	1
Thickness between channels (mm)	3
Frontal plate thickness (mm)	1.5

different temperature ranges: medium temperature (100 °C-150 °C) and high temperature (200 °C-250 °C).

The solar collection subsystem consists of a primary mirror field, which concentrates the sunlight on the receiver located at the top in the focus axis. The primary mirror data are taken from LF-11 collector [6]. The mirror field and the solar flux map on the absorber panels are computed by means of the Soltrace software [23]. This program performs a Monte Carlo ray tracing, obtaining the optical efficiency, as well as the incident flux map. All calculations have been made for the design-point conditions and considering that sun rays fall vertically. These conditions, as well as the main parameters of the primary mirror field, are summarised in Table 3.

2.3. Objective functions for the thermal optimisation

The objective functions for the thermal optimisation are the exergy and the energy efficiencies of the solar receiver, given by Eq. (5) and Eq. (6), respectively.

$$\eta_{ex,receiver} = \frac{\Delta Ex_{CO2,receiver}}{\Delta Ex_{solar,receiver}} \tag{5}$$

$$\eta_{en,receiver} = \frac{\dot{Q}_{th,CO2,receiver}}{\dot{Q}_{solar,receiver}} \tag{6}$$

In the above equations, $\dot{Q}_{solar,receiver}$ is the total incident solar radiation on the receiver, while $\Delta Ex_{solar,receiver}$ is the exergy associated to this incident solar radiation [13]; $\dot{Q}_{th,CO2,receiver}$ is the thermal gain by the CO_2, given by Eq. (7); finally, as the CO_2 in the receiver is far enough from the critical point, ideal gas behaviour is assumed, so the exergy gain is modelled by Eq. (8).

Table 3
Parameters for the primary mirror field calculation.

Design point conditions	
Direct Normal Irradiation, DNI (W m^{-2})	950
Ambient temperature (°C)	25
Effective sky temperature (°C)	15
Wind velocity (m s^{-1})	2
Geometrical and optical parameters for the primary mirror field	
Number of primary mirrors	16
Total solar field width (m)	16
Primary reflective surface width (m)	12
Filling factor	0.75
Primary mirror width (m)	0.75
Primary mirror height above ground level (m)	1.2
Receiver height above primary reflective surface (m)	7.4
Mirror axis orientation	N–S
Mirror reflectivity	0.93

$$\dot{Q}_{th,CO2,receiver} = \dot{m} \cdot \left[(h_{out} - h_{in}) + \frac{1}{2} \cdot \left(v_{out}^2 - v_{in}^2 \right) \right] \quad (7)$$

$$\Delta Ex_{CO2,receiver} = \dot{m} \cdot \left[\Delta h \left(1 - \frac{T_{amb}}{T_{LMTD}} \right) + R \cdot T_{amb} \cdot \ln \left(\frac{P_{out}}{P_{in}} \right) \right] \quad (8)$$

where T_{amb} is the ambient temperature; T_{LMTD} is the log mean temperature difference between the outlet and inlet of each receiver element along the fluid flow direction; R is the ideal gas constant; and P is the fluid pressure, at the inlet and outlet of each receiver element.

At last, a parametric analysis is achieved by considering the optics of the LFC system, using an optical efficiency calculated with Soltrace, η_{opt}, and extending the above variables to the entire solar subsystem, Eq. (9) and Eq. (10).

$$\eta_{ex,solar\_subsystem} = \eta_{opt} \cdot \eta_{ex,receiver} \quad (9)$$

$$\eta_{en,solar\_subsystem} = \eta_{opt} \cdot \eta_{en,receiver} \quad (10)$$

3. Results and discussion

3.1. Thermal performance optimisation as a function of the cavity aperture half-angle shaped by the absorber panels

This first comparative study has focused on the macroscopic configuration of the receiver, analysing the light-trapping geometry feature. For this purpose, the LFC thermal power, and both the absorber panel and the channel dimensions are fixed; and the cavity aperture half-angle is ranged between the values shown in Table 4.

As seen in Fig. 4, the LFC optical efficiency (η_{opt}) declines as the aperture half-angle decreases, due to the reduced number of impacts of the reflected solar rays on the absorber panels. This effect is very important, and particularly pronounced when the aperture half-angle is lower than 50°. In the same figure, the receiver energy efficiency ($\eta_{en,receiver}$) is depicted as function of the aperture angle, for two thermal fluid working temperature ranges: medium temperature (100 °C-150 °C) and high temperature (200 °C-250 °C). As expected, the receiver energy efficiency at high temperature is lower than at low temperature, as the thermal losses are greater as the temperature increases. In addition, for each case, the receiver energy efficiency increases with lower aperture angle, mainly due to the enhanced effect of the light-trapping geometry; this fact will be discussed in depth in the following paragraphs of this section. From a quantitative viewpoint, it is noticeable that this improvement is smaller than the optical efficiency reduction, so the total LFC energy efficiency ($\eta_{en,LFC}$), which is a convolution of both curves, follows a similar shape than the optical efficiency curve. The optical efficiency is almost constant at the beginning, while the total energy efficiency slightly increases at the beginning, it reaches a maximum, and then it decreases. In the case of the total LFC energy efficiency for high temperature (200 °C-250 °C), the maximum is reached at an opening half-angle of 75°, while for medium temperature, the maximum is reached at 80°. Although the difference between these two values is small, as the working temperature increases and the thermal losses become greater, a smaller aperture half-angle is preferred, to enhance the effect of the light-trapping geometry.

Comparing the values of the LFC efficiency shown in Fig. 4 with those provided in the LF-11 technical datasheet [6], it can be observed that for a temperature increase between 100 °C and 150 °C, the LFC efficiency values are similar, around 68%. However, as the working temperature rises, the LFC efficiency for the microchannel receiver concept decreases to a greater extent than that of the evacuated single-tube receiver design. This is primarily attributed to the better optical characteristics of the selective coating in the latter. Nevertheless, the microchannel receiver exhibits higher robustness and cost-effectiveness. Moreover, it can operate at even higher temperatures above 400 °C without degradation of the working fluid (which is a gas) or the selective coating.

Fig. 5 shows the exergy efficiency evolution, for the two previous cases. Contrary to what happened with the energy efficiency, the exergy efficiency increases as the working temperature is higher. For each case, an evolution similar to the previous one is observed, in which the total LFC exergy efficiency ($\eta_{ex,LFC}$) follows the optical efficiency evolution, previously represented in Fig. 4. Although the maximum is not obvious, the highest exergy efficiency is also identified for each case, which corresponds to an aperture half-angle of 75° for the medium temperature case (100 °C-150 °C), and 70° for the high temperature case (200 °C-250 °C). As in the energy efficiency, the maximum shifts towards smaller opening angles as the working temperature increases and the heat losses are greater, since the effect of the light-trapping is more significant.

Table 4
Fixed and variable parameters for the comparative analysis as function of the cavity aperture half-angle.

Fixed parameters	
Thermal power (MW_{th})	0.1
Channel side for pass 1 (mm)	9
Channel side for pass 2 (mm)	5
Number of channels along panel thickness	6
Number of channels along pass 1 width	16
Number of channels along pass 2 width	25
Variable parameters	
Cavity aperture half-angle (degrees)	10 - 90 (Horizontal)
Temperature increment (°C)	(100–150); (200–250)

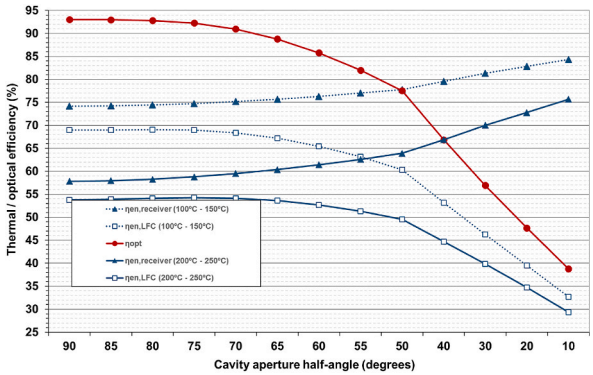

Fig. 4. Energy and optical efficiencies for the receiver and the LFC, as a function of the cavity aperture half-angle.

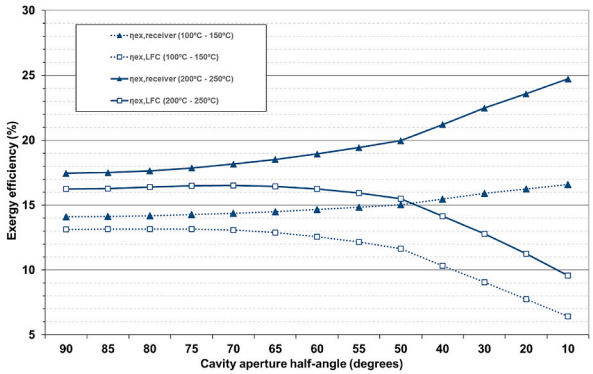

Fig. 5. Exergy and optical efficiencies for the receiver and the LFC, as a function of the cavity aperture half-angle.

Table 5 provides a more comprehensive list of the heat losses and pressure drop for each case studied, including the LFC length. As the receiver energy efficiency increases with smaller aperture half-angles, the length required to achieve the same thermal power (0.1 MW_{th}) decreases, and the pressure drop is reduced. This explains why the exergy efficiency, shown in Fig. 5, presents a maximum value for an aperture half-angle slightly lower than the one corresponding to the maximum energy efficiency: smaller aperture half-angles result in lower pressure drop.

To conclude this section, an in-depth study of the heat losses is explained, comparing the heat losses from the absorber surface corresponding to pass 1 and those corresponding to pass 2. This evolution is represented in Fig. 6.

As seen in Fig. 6, for most of the cavity opening angles, the heat losses from the panel area corresponding to pass 2 are higher than those from pass 1, which is caused by two phenomena: the working fluid temperature is higher and, for a standard pointing strategy to the LFC focal line, the concentrated solar radiation is higher on the panel area corresponding to pass 2 than on the one corresponding to pass 1.

Table 5
Heat losses and pressure drop of the LFC, as a function of the aperture half-angle of the cavity shaped by the absorber panels.

Aperture half-angle (degrees)	$T_{inlet} = 100$ °C; $T_{outlet} = 150$ °C			$T_{inlet} = 200$ °C; $T_{outlet} = 250$ °C		
	LFC Length (m)	Heat Loss (kW_{th})	Pressure Drop (bar)	LFC Length (m)	Heat Loss (kW_{th})	Pressure Drop (bar)
90 (Horizontal)	19.02	17.52	1.24	24.70	37.11	2.00
85	19.01	17.46	1.24	24.65	36.93	2.00
80	18.95	17.27	1.23	24.50	36.42	1.99
75	18.86	16.97	1.23	24.26	35.61	1.97
70	18.75	16.58	1.22	23.96	34.55	1.95
65	18.62	16.12	1.22	23.59	33.29	1.92
60	18.47	15.58	1.21	23.17	31.85	1.89
55	18.29	14.98	1.20	22.71	30.27	1.85
50	18.11	14.32	1.18	22.22	28.58	1.81
40	17.70	12.90	1.16	21.19	25.00	1.73
30	17.30	11.50	1.14	20.20	21.58	1.65
20	16.98	10.38	1.13	19.40	18.81	1.60
10	16.67	9.30	1.12	18.64	16.15	1.55

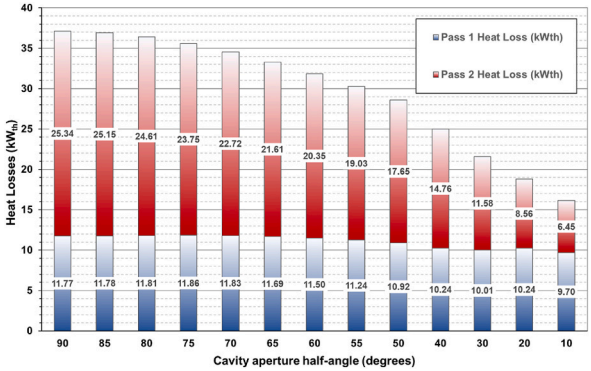

Fig. 6. Heat losses from pass 1 and pass 2 absorber panel surface, as function of the cavity aperture half-angle.

The heat losses from each pass of the panel decrease for smaller cavity opening angles; however, this reduction is much more pronounced for pass 2 compared to pass 1, which is explained by two reasons. The first reason is that the view factor from the absorber surface to the outside decreases when the aperture angle is reduced; this reduction is greater for pass 2 compared to pass 1, because pass 2 is located in the inner part of the cavity, close to the focal axis. The evolution of the view factors is shown in Table 6.

The second reason for the greater reduction in heat losses from pass 2 compared to pass 1 is found in the solar flux map evolution on the absorber surface as the cavity opening angle is reduced. Fig. 7 shows the flux map for an opening half-angle equal to 90° (horizontal panel), compared to the case with an opening half-angle of 10°. In the first case, the solar flux peak is located close to the focal line. However, in the second case, the panel inclination causes the sun's rays to impinge the absorber panel area close to the aperture rather than the area close to the focal line, so the solar flux peak is shifted from the inner area, close to the focal line, to the outer area, close to the aperture.

3.2. Thermal performance optimisation as function of the channel dimensions for each pass

This second comparative analysis is focused on the internal structure of the microchannel absorber panel and its main feature of gradual compactness. For this purpose, the external position of the panels comprising the receiver, and the global configuration of the LFC are fixed, as shown in Table 5. Specifically, the configuration that leads to the highest exergy efficiency working in the temperature range 200 °C - 250 °C is chosen, calculated in the previous section. In that case, the optimum configuration corresponds to a value of 70° for the cavity aperture half-angle.

For this comparison, the side of the quadrangular channel is varied, for both pass 1 and pass 2, in the range of values shown in Table 7. To clearly show the impact of the thermal resistance values, the total number of channels of the absorber panel is kept constant (i.e. the number of channels along the thickness of the panel and along the width of pass 1 and pass 2).

By keeping the number of channels constant, the panel thickness and width increase when the channel side is increased. The panel width variation affects the concentrated solar radiation map on the absorber surface and the LFC optical efficiency, which has been calculated again by Soltrace, for different panel widths and 70° tilt, as shown in Table 8. For each specific width, it is interpolated in the range of values listed in this table.

As shown in Fig. 8a, the heat losses increase as the channel dimensions increase. This is because, as the channel dimensions increase while keeping the number of channels constant, the mass flow rate per channel decreases, thus decreasing the convection heat transfer coefficient. This causes the thermal resistance to increase through the panel thickness, increasing the external surface temperature of the panel, which leads to higher pressure drop. On the other hand, as shown in Fig. 8b, the pressure drop follows an opposite trend: it decreases by decreasing the channel velocity, i.e. by increasing the channel dimensions.

This opposite trend of heat losses and pressure drop is not captured by the LFC energy efficiency (Fig. 9a), which follows a similar pattern of variation as heat loss, with the thermal efficiency increasing as the heat losses decrease. However, the LFC exergy efficiency (Fig. 9b) does account for both the heat losses and pressure drop, showing a maximum in the following range of values for the quadrangular channel side: (9 mm–10 mm) for pass 1; and (5 mm–6.5 mm) for pass 2.

The same Fig. 9b clearly shows the advantage of using different compactness for pass 1 and pass 2, compared to using the same channel dimensions for both passes. As seen in this figure, the region with the same compactness (between 7 mm and 9 mm, for both passes) presents efficiencies between 8.5% and 16.5%, far away from the maximum (18.5%).

4. Conclusions and recommendations

This paper presents the design of a microchannel receiver for LFC systems using pressurised gas as working fluid. The receiver consists of two absorber panels converging at the focal axis, shaping a cavity with a triangular cross-section that performs as a light-trapping geometry characterised by the aperture half-angle. The working fluid flows through each panel in several passes, so that the compactness of the microchannel structure is constant in each pass and greater than in the previous pass. The advantages of this design include its simplicity, its robustness, and its ability to provide high-temperature heat for industrial processes.

A comparative study has been carried out based on the characteristic parameters of this receiver design, seeking to maximise the

Table 6
View factor from pass 1 and pass 2 absorber panel surface to the outside, as a function of the cavity aperture half-angle.

Cavity half-angle (degrees)	View factor from the panel surface to the outside	
	Pass 1	Pass 2
90 (Horizontal)	1.00	1.00
85	1.00	0.99
80	0.99	0.98
75	0.98	0.95
70	0.96	0.92
65	0.94	0.88
60	0.91	0.82
55	0.88	0.76
50	0.84	0.69
40	0.75	0.54
30	0.63	0.37
20	0.49	0.20
10	0.29	0.06

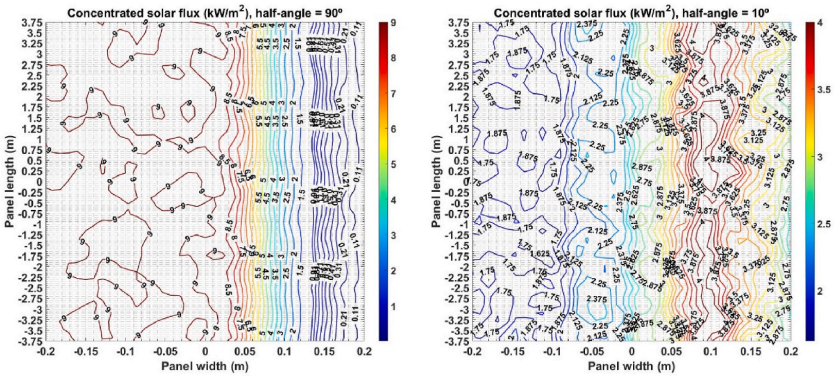

Fig. 7. Concentrated solar flux map on the absorber panel surface, for a cavity aperture half-angle equal to 90° (on the left) and equal to 10° (on the right).

Table 7
Fixed and variable parameters for the comparative analysis as function of the channel dimensions.

Fixed parameters	
Thermal power (MW_{th})	0.1
Temperature increment (°C)	200–250
Cavity aperture half-angle	70
Number of channels along panel thickness	6
Number of channels along pass 1 width	16
Number of channels along pass 2 width	25
Variable parameters	
Channel side for pass 1 (mm)	7–12
Channel side for pass 2 (mm)	4–9

Table 8
Optical efficiency as function of the absorber panel width, for a cavity aperture half-angle of 70°.

Panel width (m)	Optical efficiency (%)
0.33	87.66
0.35	88.84
0.37	89.83
0.39	90.62
0.41	91.26
0.43	91.78
0.45	92.17
0.47	92.45
0.49	92.67

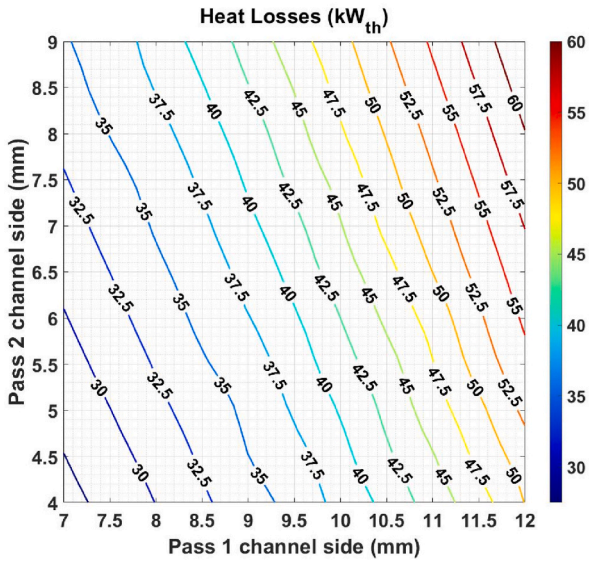

Fig. 8a. Total heat losses from the receiver absorber surface, as a function of the channel dimensions in pass 1 and pass 2.

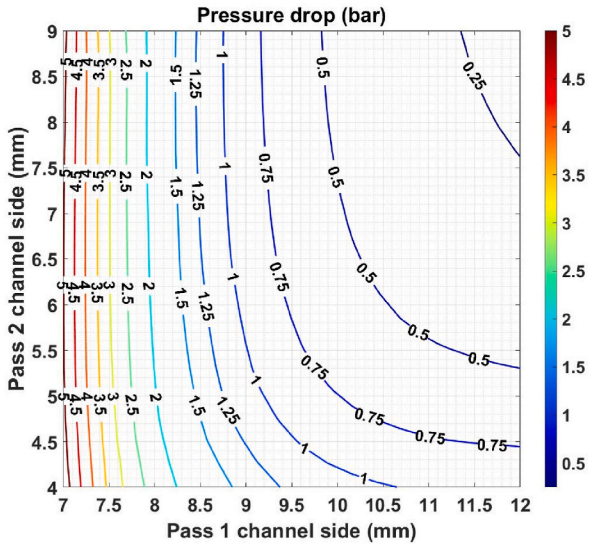

Fig. 8b. Pressure drop of the fluid through the receiver, as a function of the channel dimensions in pass 1 and pass 2.

exergy efficiency. As a result of this analysis, the following outcomes are highlighted.

- There is an aperture half-angle value for which the LFC exergy efficiency is maximum, resulting of two opposite effects: the optical efficiency reduction as the aperture half-angle decreases; and the lower heat losses for smaller aperture half-angles, which enhance the light-trapping effect. For the specific case under study, this maximum is achieved for a cavity aperture half-angle of 70°, although it depends on many factors, such as the working temperature, the heat transfer fluid or the type of compact geometry.
- The increasing compactness of the microchannel structure in each absorber panel, improves its energy and exergy efficiency, compared to a panel in which the channel dimensions were kept constant in all the passes. It is also found that, from a thermal point of view, it is worthwhile to use smaller channels to improve the panel cooling and reduce heat losses. However, if the pressure drop is considered via the exergy efficiency, it is possible to identify a maximum, resulting of two opposite effects: the lower heat losses as the velocity increases, and the higher pressure drop at higher velocities. This maximum will depend on each specific case, and in this case is in the following range of channel side: (9 mm–10 mm) for pass 1; and (5 mm–6.5 mm) for pass 2.

The main limitations of the microchannel receiver presented in this work are related to materials and storage possibility. Regarding materials, the main drawback is that materials that can withstand higher temperatures usually have a lower thermal conductivity, which increases the thermal gradient along the thickness of the panel. Regarding storage, this is a common challenge for all solar

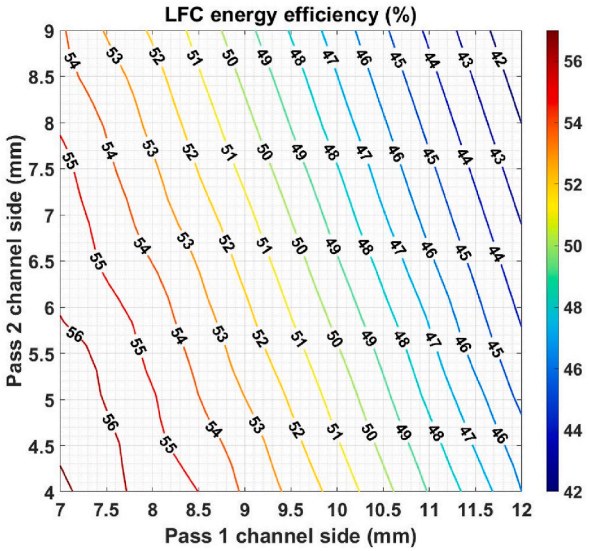

Fig. 9a. LFC energy efficiency, as a function of the channel dimensions in pass 1 and pass 2.

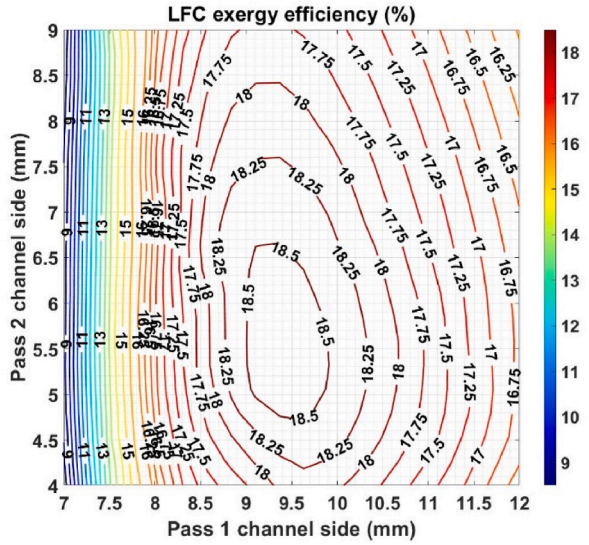

Fig. 9b. LFC exergy efficiency, as a function of the channel dimensions in pass 1 and pass 2.

thermal technologies. Although the most conventional storage is molten salt tanks, the optimal solution would be to develop specific storage for gases, in pebble-beds or something similar.

In line with the limitations described above, future recommendations would focus primarily on research into new materials, such as ceramic materials, which can operate at high temperature with relatively high thermal conductivity. In addition, the development of specific storage systems for gaseous fluids would be an improvement to the technology. Finally, several future research lines relating to the receiver design improvement can be defined, such as: thermo-mechanical analysis of the receiver using finite elements; simulation of other types of geometries for the core fin: plain triangular fin, wavy fin, offset strip fin, perforated fin and louvred fin; and the use of other gases at different pressures.

CRediT author statement

María José Montes: term; conceptualization; methodology; software; formal analysis; validation; investigation; resources; data curation; writing – original draft; writing – review & editing; visualization; supervision; funding acquisition; project administration, Valentina Stojceska: term; conceptualization; methodology; investigation; formal analysis; investigation; resources; writing – original draft; writing – review & editing; David Reay: term; conceptualization; methodology; software; formal analysis; validation;

investigation; resources; data curation; writing – review & editing; visualization; funding acquisition, Mercedes Ibarra: term; conceptualization; investigation; resources; writing – review & editing.

Declaration of competing interest

The authors declare the following financial interests/personal relationships which may be considered as potential competing interests:

Maria Jose Montes reports financial support was provided by Horizon Europe. Maria Jose Montes has patent #Receptor solar constituido por paneles absorbedores basados en estructuras compactas. Spanish Patent Application No. P202131189 issued to ES2911108. No. PCT/ES2022/070,705.

Data availability

Data will be made available on request.

Acknowledgments

This work has been developed in the frame of the ASTEP project, funded by the European Union's Horizon 2020 research programme under grant agreement N°884411. Disclosure: The present publication reflects only the author's views and the European Union are not liable for any use that may be made of the information contained therein.

References

[1] L. Kumar, M. Hasanuzzaman, N.A. Rahim, Global advancement of solar thermal energy technologies for industrial process heat and its future prospects: a review, Energy Convers. Manag. 195 (2019) 885–908, https://doi.org/10.1016/j.enconman.2019.05.081.
[2] P. Horta, Technical Report A.1.3: Process Heat Collectors: State of the Art and Available Medium Temperature Collectors, 2016. https://task49.iea-shc.org/publications.
[3] G. Zhu, T. Wendelin, M.J. Wagner, C. Kutscher, History, current state, and future of linear Fresnel concentrating solar collectors, Sol. Energy 103 (2014) 639–652, https://doi.org/10.1016/j.solener.2013.05.021.
[4] M.J. Montes, R. Barbero, R. Abbas, A. Rovira, Performance model and thermal comparison of different alternatives for the Fresnel single-tube receiver, Appl. Therm. Eng. 104 (2016) 162–175, https://doi.org/10.1016/j.applthermaleng.2016.05.015.
[5] SolarPaces (2022). https://www.solarpaces.org/.
[6] Technical datasheet for LF11: https://www.industrial-solar.de/en/technologies/fresnel-collector/.
[7] D. Mills, Advances in solar thermal electricity technology, Sol. Energy 76 (2004) 19–31, https://doi.org/10.1016/S0038-092X(03)00102-6.
[8] A. Soum-Glaude, I. Bousquet, M. Bichotte, S. Quoizola, L. Thomas, G. Flamant, Optical characterization and modeling of coatings intended as high temperature solar selective absorbers, Energy Proc. 49 (2014) 530–537, https://doi.org/10.1016/j.egypro.2014.03.057.
[9] Q. Li, G. Flamant, X. Yuan, P. Neveu, L. Luo, Compact heat exchangers: a review and future applications for a new generation of high temperature solar receivers, Renew. Sustain. Energy Rev. 15 (2011) 4855–4875, https://doi.org/10.1016/j.rser.2011.07.066.
[10] S.M. Besarati, D.Y. Goswami, E.K. Stefanakos, Development of a solar receiver based on compact heat exchanger technology for supercritical Carbon Dioxide power cycles, J. Sol. Energy Eng. 137 (2015), 031018, https://doi.org/10.1115/1.4029861.
[11] S.D. Sullivan, J. Kesseli, J. Nash, J. Farias, D. Kesseli, W. Caruso, High-Efficiency Low-Cost Solar Receiver for Use Ina a Supercritical CO2 Recompression Cycle (No. DOE-BRAYTON–0005799, 1333813), 2016, https://doi.org/10.2172/1333813.
[12] M.J. Montes, R. Guédez, D. D'Souza, J.I. Linares, J. González-Aguilar, M. Romero, Proposal of a new design of central solar receiver for pressurised gases and supercritical fluids, Int. J. Therm. Sci. 194 (2023), 108586, https://doi.org/10.1016/j.ijthermalsci.2023.108586.
[13] D. D'Souza, M.J. Montes, M. Romero, J. González-Aguilar, Energy and exergy analysis of microchannel central solar receivers for pressurised fluids, Appl. Therm. Eng. 219 (2023), 119638, https://doi.org/10.1016/j.applthermaleng.2022.119638.
[14] M.J. Montes, D. D'Souza, J.I. Linares, J. González-Aguilar, A. Rovira, M. Romero, Proposal of a Microchannel Receiver for Pressurised Fluids Based on Different Compact Geometries, Presented at the SOLARPACES 2022: International Conference on Concentrating Solar Power and Chemical Energy Systems, Albuquerque, USA, 2022.
[15] Q. Li, G. Flamant, X. Yuan, P. Neveu, L. Luo, Compact heat exchangers: a review and future applications for a new generation of high temperature solar receivers, Renew. Sustain. Energy Rev. 15 (2011) 4855–4875, https://doi.org/10.1016/j.rser.2011.07.066.
[16] M.J. Montes, A. Rovira, J. González-Aguilar, M. Romero, Spanish Patent Application No. 202131189, 2021.
[17] M.M. Rodríguez, J.M. Márquez, M. Biencinto, J.P. Adler, L.E. Díez, First experimental results of a solar PTC facility using gas as the heat transfer fluid, in: SolarPACES 2009 Conference, 2009. Berlin, Germany.
[18] M. Biencinto, L. González, E. Zarza, L.E. Díez, J. Muñoz-Antón, Performance model and annual yield comparison of parabolic-trough solar thermal power plants with either nitrogen or synthetic oil as heat transfer fluid, Energy Convers. Manag. 87 (2014) 238–249, https://doi.org/10.1016/j.enconman.2014.07.017.
[19] MATLAB & Simulink – MathWorks, 2022. https://matlab.mathworks.com.
[20] J.E. Hesselgreaves, Compact Heat Exchangers: Selection, Design, and Operation, second ed., Elsevier/BH, Amsterdam, 2017.
[21] NIST database https://webbook.nist.gov/chemistry/.
[22] A. Rodríguez-Palomo, E. Céspedes, D. Hernández-Pinilla, C. Prieto, High-temperature air-stable solar selective coating based on MoSi2–Si3N4 composite, Sol. Energy Mater. Sol. Cell. 174 (2018) 50–55, https://doi.org/10.1016/j.solmat.2017.08.021.
[23] T. Wendelin, SolTRACE: A New Optical Modeling Tool for Concentrating Solar Optics. Proceedings of the ISEC 2003: International Solar Energy Conference, 15-18 March 2003, Kohala Coast, Hawaii, American Society of Mechanical Engineers, New York, 2003, pp. 253–260. NREL Report No. CP-550-32866.